

# Three-dimensional streaming flow in confined geometries

Bhargav Rallabandi<sup>1,†</sup>, Alvaro Marin<sup>2</sup>, Massimiliano Rossi<sup>2</sup>,  
Christian J. Kähler<sup>2</sup> and Sascha Hilgenfeldt<sup>1</sup>

<sup>1</sup>Department of Mechanical Science and Engineering, University of Illinois at Urbana-Champaign,  
1206 West Green Street, Urbana, IL 61801, USA

<sup>2</sup>Institute for Aerodynamics and Fluid Mechanics, Bundeswehr University Munich,  
85577 Neubiberg, Germany

(Received 16 December 2014; revised 7 April 2015; accepted 12 June 2015;  
first published online 20 July 2015)

Steady streaming vortex flow from microbubbles has been developed into a versatile tool for microfluidic sample manipulation. For ease of manufacture and quantitative control, set-ups have focused on approximately two-dimensional flow geometries based on semi-cylindrical bubbles. The present work demonstrates how the necessary flow confinement perpendicular to the cylinder axis gives rise to non-trivial three-dimensional flow components. This is an important effect in applications such as sorting and micromixing. Using asymptotic theory and numerical integration of fluid trajectories, it is shown that the two-dimensional flow dynamics is modified in two ways: (i) the vortex motion is punctuated by bursts of strong axial displacement near the bubble, on time scales smaller than the vortex period; and (ii) the vortex trajectories drift over time scales much longer than the vortex period, forcing fluid particles onto three-dimensional paths of toroidal topology. Both effects are verified experimentally by quantitative comparison with astigmatism particle tracking velocimetry (APTV) measurements of streaming flows. It is further shown that the long-time flow patterns obey a Hamiltonian description that is applicable to general confined Stokes flows beyond microstreaming.

**Key words:** bubble dynamics, low-Reynolds-number flows, microfluidics

## 1. Introduction

Oscillations of a boundary relative to surrounding viscous fluid can give rise to secondary steady currents. These steady flows, driven by non-zero Reynolds stresses due to the inertia of the fluid oscillation, have been termed (boundary) ‘streaming flows’ and are observed in a wide variety of applications (Longuet-Higgins 1953; Nyborg 1958; Lighthill 1978). Classical studies of such streaming phenomena have focused on translational oscillations of solids (Raney, Corelli & Westervelt 1954; Riley 1965, 1966; Stuart 1966). More recently there has been increased interest in streaming due to bubbles undergoing a combination of volume and shape oscillations, primarily for two reasons: (a) bubbles allow a more powerful actuation of the

† Email address for correspondence: [rallaba2@illinois.edu](mailto:rallaba2@illinois.edu)

flow due to the large amplitudes that may be accessed (the streaming speed being quadratic in the oscillation amplitude) and (b) flows over bubbles, which generally permit slip, are subject to little frictional resistance compared to those over solid no-slip surfaces. This makes acoustically excited bubbles particularly attractive for microfluidics, where they have been successfully used for applications such as particle trapping (Lutz, Chen & Schwartz 2006; Wang, Jalikop & Hilgenfeldt 2011; Rogers & Neild 2011), size-selective sorting (Wang, Jalikop & Hilgenfeldt 2012), shear force actuation (Marmottant & Hilgenfeldt 2003) and microfluidic mixing (Liu *et al.* 2002; Ahmed *et al.* 2009; Wang *et al.* 2009; Wang, Rallabandi & Hilgenfeldt 2013).

In order to obtain streaming flows that are not only powerful, but conceptually simple and easy to manufacture in a microfluidic context, initial work on hemispherical bubbles (Marmottant & Hilgenfeldt 2003, 2004) has widely been replaced by a two-dimensional geometry (Wang *et al.* 2011; Patel, Tovar & Lee 2012; Wang *et al.* 2012; Wiklund, Green & Ohlin 2012; Xie *et al.* 2012; Phan *et al.* 2014): in such microstreaming devices, the bubble has a semi-cylindrical shape and is sessile on the wall of the device (see figure 1*a*). The bubble is confined axially by two parallel walls (henceforth called top and bottom walls), which establishes a stable interface attached to the device by means of pinned contact lines. It has been shown that the symmetry of the set-up establishes approximately two-dimensional flows close to the mid-plane of the channel (where the flow is fastest) (Rallabandi, Wang & Hilgenfeldt 2014). The two-dimensional theory, however, must have limitations close to the top and bottom walls of the channel, where the flow speed approaches zero. It is important to quantify any three-dimensional flow effects, which may affect applications such as mixing or sorting either beneficially or adversely. Until now, no study has developed a systematic theory of three-dimensional streaming.

In the present work, we build on our own two-dimensional streaming theory, and show that the presence of the top and bottom walls, together with the oscillatory properties of the bubble surface, introduce characteristic secondary axial flow components that are not confined to the vicinity of the walls, but introduce qualitative changes to the entire flow field. The superposition of the primary two-dimensional streaming and the secondary axial flows results in a three-dimensional flow field that explains recent experimental particle trajectory data measured by astigmatism particle tracking velocimetry (APT) experiments (Cierpka *et al.* 2011; Marin *et al.* 2015). We show how our theory describes new aspects of particle motion in streaming flows over both short and long time scales, adding important new insight. The results are then generalized to any simple superposition of two-dimensional and axisymmetric flow components in the framework of a Hamiltonian flow theory on long time scales, establishing a broader applicability to general axially confined two-dimensional flows.

## 2. Problem definition and governing equations

Figure 1 illustrates the typical geometry of a microbubble used to drive streaming flows in a microfluidic device: the semi-cylindrical bubble of radius  $a$  protrudes from a blind side channel of width  $2a$  branching off a main channel, whose opposite wall (in the  $y$ -direction) is at a distance of  $H = ha$ . The entire structure has a uniform depth  $D = da$  in the  $z$ -direction for ease of manufacture, so that the bubble axis spans the depth of the microchannel, see figure 1(*a*). The bubble contact lines at  $(x = \pm a, y = 0)$  are pinned to the side channel corners. The channel is filled with a fluid of kinematic viscosity  $\nu$  and density  $\rho$ . The application of an acoustic driving pressure at an angular frequency  $\omega = 2\pi f$  (via a piezoelectric transducer) drives harmonic oscillations of

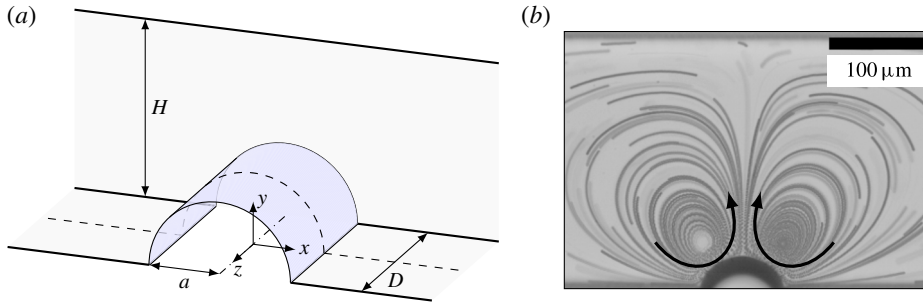


FIGURE 1. (Colour online) (a) Geometry of the microchannel, showing the bubble and the coordinate system. (b) Experimental flow lines in a  $d=2.5$ ,  $h=6.25$  channel showing the predominant two-dimensional ‘fountain mode’ streaming (indicated by arrows), visualized using signals from tracer particles of  $2\ \mu\text{m}$  diameter in a region of  $\sim 10\ \mu\text{m}$  around the channel mid-plane ( $z=0$ ).

the bubble surface at a characteristic amplitude  $\epsilon a$ , where  $\epsilon \ll 1$ . Note that for the typical sizes ( $a \sim 50\ \mu\text{m}$ ) and frequencies ( $f \sim 20\ \text{kHz}$ ) the acoustic wavelength is much greater than the bubble size. Using  $a$  and  $\omega^{-1}$  to normalize length and time respectively, the interface shape for small-amplitude oscillations can in general be written as

$$R(\theta, z, t) = 1 - i\epsilon e^{it}\zeta(\theta, z), \quad (2.1)$$

where  $\zeta(\theta, z)$  is a complex function and it is understood that only the real part of any complex expression has physical significance. Here,  $\theta = \tan^{-1}(y/x)$  is the polar angle. Oscillations of the interface drive a flow field which, in the limit of small oscillation amplitude, is conveniently solved for by an expansion in powers of  $\epsilon$  (Riley 1967; Davidson & Riley 1971; Longuet-Higgins 1998; Riley 2001; Sadhal 2012; Rallabandi *et al.* 2014).

The primary oscillatory flow  $\mathbf{u}_0$  (characteristic scale  $\epsilon a\omega$ ) is irrotational except in viscous boundary layers of dimensionless thickness  $\delta \equiv a^{-1}\sqrt{2\nu/\omega} \ll 1$ , near the boundaries of the domain (Longuet-Higgins 1953; Nyborg 1958; Longuet-Higgins 1998). Steady Reynolds stresses due to the oscillatory flow drive a secondary steady Eulerian flow  $\langle \mathbf{u}_1 \rangle$  ( $\langle \cdot \rangle$  denotes the time average over an oscillation cycle), with a characteristic velocity scale  $u_s = \epsilon^2 a\omega$  and a streaming Reynolds number  $Re_s = u_s a/\nu$ , which is  $\ll 1$  in many practical situations (Nyborg 1958; Wu & Du 1997; Longuet-Higgins 1998; Riley 2001), including microfluidics applications (Wang *et al.* 2011, 2013; Sadhal 2012). The time-averaged motion of fluid elements under the combination of the primary and secondary flows can be described in terms of a steady Lagrangian velocity field  $\mathbf{U} = \langle \mathbf{u}_1 \rangle + \mathbf{u}_d$ , where  $\mathbf{u}_d$  is the Stokes drift, defined by

$$\mathbf{u}_d = \left\langle \left( \int \mathbf{u}_0 dt \cdot \nabla \right) \mathbf{u}_0 \right\rangle. \quad (2.2)$$

It is this time-averaged Lagrangian motion of the fluid that is practically relevant for fluid transport and is normally referred to as the ‘steady streaming’. Figure 1(b) shows the typical appearance of the steady streaming flow from a sessile bubble as viewed along the axis of the bubble. It was observed experimentally (Wang 2013; Wang *et al.* 2013) and shown theoretically (Rallabandi *et al.* 2014) that this pattern of a vortex pair in ‘fountain’ orientation (flow upwards at  $x=0$ ) persists virtually

unchanged over a range of frequencies. It was also observed (Wang 2013) that the pattern does not vary much with the depth  $z$  (compare out-of-focus tracks with the in-focus tracks closer to  $z = 0$ , in figure 1*b*). However, the latter observations of the two-dimensional character of the flow were limited by the microscopic depth of field ( $\gtrsim 10 \mu\text{m}$ ) and the general inability to follow individual particles over long times. We will show here that new flow features appear beyond two-dimensional flow, and that they can be verified by more sophisticated experimental techniques.

For a theoretical description of the streaming  $\mathbf{U}$ , it is convenient to first write the Reynolds stress term  $\boldsymbol{\sigma} \equiv \langle \mathbf{u}_0 \cdot \nabla \mathbf{u}_0 \rangle$  as  $\boldsymbol{\sigma} = \langle \nabla |\mathbf{u}_0|^2 / 2 \rangle + \langle (\nabla \times \mathbf{u}_0) \times \mathbf{u}_0 \rangle$ . Using the viscous stress scale  $\rho \nu u_s / a$  to non-dimensionalize the time-averaged pressure, the dimensionless governing equations for the Lagrangian steady flow in the limit  $Re_s \ll 1$  are

$$\left. \begin{aligned} \nabla \cdot \mathbf{U} &= 0, \\ \nabla^2 \mathbf{U} &= \nabla^2 \mathbf{u}_d + \nabla p + \mathbf{f}, \end{aligned} \right\} \quad (2.3)$$

where

$$p = \langle p_1 \rangle + \frac{2}{\delta^2} \left\langle \frac{|\mathbf{u}_0|^2}{2} \right\rangle, \quad \text{and} \quad \mathbf{f} = \frac{2}{\delta^2} \langle (\nabla \times \mathbf{u}_0) \times \mathbf{u}_0 \rangle. \quad (2.4a,b)$$

Here,  $p$  is a dimensionless effective pressure that incorporates both the time-averaged fluid pressure  $\langle p_1 \rangle$  and the kinetic energy of the oscillatory flow, and  $\mathbf{f}$  is a body force related to the advection of oscillatory vorticity, which is confined to viscous boundary layers (Riley 2001). The Lagrangian mean flow is no-penetration with a vanishing tangential stress at the mean bubble surface  $\partial\Omega_b$ , and satisfies no-slip boundary conditions at the rigid wall surfaces  $\partial\Omega_w$ ,

$$\left. \begin{aligned} \mathbf{U} &= 0 \quad \text{on } \partial\Omega_w \\ U_r &= 0 \quad \text{on } \partial\Omega_b \\ \mathbf{S}_{r\theta} = \mathbf{S}_{rz} &= 0, \quad \text{on } \partial\Omega_b, \end{aligned} \right\} \quad (2.5)$$

where  $\mathbf{S}$  is the symmetric part of  $\nabla \mathbf{U}$ . Outside viscous boundary layers, where  $\mathbf{f}$  is exponentially small, the Eulerian steady flow  $\langle \mathbf{u}_1 \rangle = \mathbf{U} - \mathbf{u}_d$  satisfies the Stokes equations, supported by the effective pressure  $p$ .

### 3. Axial streaming

To motivate the streaming solutions that will be developed in this section, we first provide the general form of the oscillatory flow  $\mathbf{u}_0$ , which ultimately drives (2.3) through the Reynolds stress and the Stokes drift. For typical practical applications,  $\delta \ll 1$ , allowing  $\mathbf{u}_0$  to be evaluated using matched asymptotic expansions, with an ‘outer’ potential flow outside boundary layers and ‘inner’ (viscous boundary layer) solutions described by the unsteady Stokes equations (Longuet-Higgins 1953; Nyborg 1958; Riley 2001). The oscillatory outer flow may in general be expressed as a modal decomposition

$$\mathbf{u}_0 = \sum_{n=0}^{\infty} \sum_{m=0}^{\infty} \mathbf{u}_0^{mn}, \quad (3.1)$$

where

$$\mathbf{u}_0^{mn} = e^{it} A_{mn} (2n\alpha \mathbf{K}'_{2m}(2n\alpha))^{-1} \nabla \varphi_{mn}, \quad (3.2)$$

and

$$\varphi_{mn} = \mathbf{K}_{2m}(2n\alpha r) \cos 2m\theta \cos 2n\alpha z \quad (3.3)$$

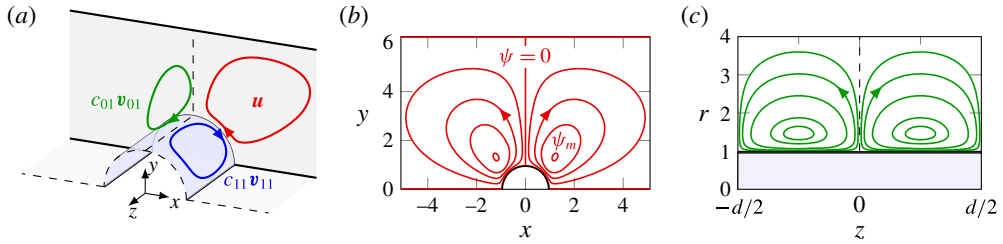


FIGURE 2. (Colour online) (a) Schematic of the flow superposition of modes in (3.18), indicating the planar fountain  $\mathbf{u}$ , the axisymmetric fountain  $c_{01}\mathbf{v}_{01}$ , and the mixed axial-azimuthal mode  $c_{11}\mathbf{v}_{11}$ . (b) Streamline portrait of the planar flow  $\mathbf{u}$  for a channel height  $h = 6.25$ , indicating limiting streamlines:  $\psi = \psi_m$  corresponds to the vortex centre of the two-dimensional flow (smallest streamline) and  $\psi = 0$ , the largest streamline. (c) Flow lines of the axisymmetric flow in an  $r$ - $z$  plane, showing a fountain orientation (radially outward velocities at  $z = 0$ ). The shaded region  $r < 1$  indicates the bubble.

is a cylindrical harmonic function ( $\nabla^2\varphi_{mn} = 0$ ). Here,  $K_\nu$  represents a modified Bessel function of the second kind, with  $K'_\nu(z) = d/dz(K_\nu(z))$  and  $\alpha \equiv \pi/d$ .  $A_{mn}$  are the (generally complex) coefficients of the Fourier decomposition of the interface deformation  $\zeta(\theta, z)$  and are determined by bubble interface dynamics and the pinning of contact lines (Wang *et al.* 2013).

Of this general combination of modes, planar modes ( $n = 0$ ) have the largest amplitudes due to their relatively small damping, driving flows that decay algebraically away from the interface. On the other hand, axial modes ( $n > 0$ ), which drive flows that decay exponentially ( $\sim e^{-2nar}$ ) away from the bubble surface are only weakly excited due to greater damping (see e.g. Sanz & Diez 1989; Wang *et al.* 2013). Therefore, to leading order, only planar modes of  $\mathbf{u}_0$  contribute to (2.3), driving two-dimensional streaming in the absence of the confining top and bottom walls (Wang *et al.* 2013; Rallabandi *et al.* 2014), see figure 2(b). Such a two-dimensional description of the flow has been used successfully to explain the experimentally observed streaming patterns and velocity fields in the  $x$ - $y$  plane in the case of oscillating bubbles (Rallabandi *et al.* 2014), cf. figure 1(b), and solid cylinders (Lutz *et al.* 2006). In general, however, steady axial flow components (in the  $z$ -direction) should be present.

Such axial velocity components of the steady streaming may be excited by two separate effects that are neglected in the two-dimensional theory: (i) the top and bottom walls necessitate that the steady fluid velocity vanish identically at the top and bottom walls ( $z = \pm d/2$ ), and (ii) axial oscillation modes of the bubble introduce Reynolds stress components that drive axial motion of the fluid.

We focus our attention on solutions of (2.3) that are valid outside steady boundary layers of thickness  $\delta \ll 1$  near the boundaries of the domain. Formally, we are interested in the outer steady solution of a matched asymptotic expansion; this will be understood henceforth unless otherwise stated. Linearity of the governing equations makes it convenient to express the (three-dimensional) Lagrangian steady velocity field  $\mathbf{U}$  as a superposition of a two-dimensional steady solution  $\mathbf{u}$  (cf. figure 2a,b) and a secondary solution  $\mathbf{v}$  with non-zero axial velocity components, i.e.

$$\mathbf{U}(r, \theta, z) = \mathbf{u}(r, \theta) + \mathbf{v}(r, \theta, z), \quad (3.4)$$

so that  $\mathbf{v}$  satisfies (2.3), with  $\mathbf{u}_d$ ,  $p$  and  $\mathbf{f}$  now taken expressly to be axially non-uniform, while planar components are addressed by  $\mathbf{u}$ .

The outer flow must also satisfy appropriate matching conditions for proper asymptotic matching with the boundary layer solutions at the mean bubble surface ( $r=1$ ) and at the top and bottom walls ( $z=\pm d/2$ ). Since normal velocity variations are small over the boundary layer thickness, kinematic boundary conditions are directly applicable to the outer solution at all boundaries  $\partial\Omega = \partial\Omega_w + \partial\Omega_b$ ,

$$\mathbf{v} \cdot \mathbf{n}_{\partial\Omega} = 0 \quad \text{on } \partial\Omega, \tag{3.5}$$

where  $\mathbf{n}_{\partial\Omega}$  is the unit normal to  $\partial\Omega$ .

No-slip conditions at the top and bottom walls are enforced with the help of steady boundary layers, which in general support large axial gradients of planar velocity components near  $z=\pm d/2$ . This establishes effective slip conditions on the Lagrangian outer flow at the top and bottom walls (generally a slip velocity of  $O(1)$ ) that depend on the particulars of the oscillatory flow  $\mathbf{u}_0$  (see e.g Longuet-Higgins 1953; Nyborg 1958). Consider now the mixed boundary layer region near the contact line at the bottom wall, defined by  $r=1+O(\delta)$ ,  $z=-d/2+O(\delta)$ , where the structure of the no-slip wall boundary layer must conform to that of the no-stress bubble boundary layer. Within this region, the pinning of contact lines, reflected in (3.5), ensures that  $U_r \sim U_z \sim O(\delta)$ , which along with no-stress conditions at the bubble ( $\partial_r(r^{-1}U_\theta) + r^{-2}\partial_\theta U_r = 0$ ), requires that  $U_\theta \sim O(\delta^2)$ . By symmetry, the same arguments are applicable to the flow in the vicinity of the contact line between the bubble and the top wall  $r=1$ ,  $z=d/2$ . All boundary layer velocity components are therefore  $O(\delta)$  or smaller in the vicinity of the contact lines at the top and bottom walls. For proper asymptotic matching, the Lagrangian outer flow must therefore, to leading order in  $\delta$ , satisfy no-slip conditions at  $r=1$ ,  $z=\pm d/2$ , which may be written as

$$\mathbf{v} = -\mathbf{u} \quad \text{on } r=1, z=\pm d/2. \tag{3.6}$$

The bubble boundary conditions are more involved, since Reynolds stresses at the bubble may in general depend on a large number of mode combinations that are sensitive to the oscillatory boundary layer structure (see e.g. Davidson & Riley 1971; Longuet-Higgins 1998; Rallabandi *et al.* 2014). Rather than compute these conditions exactly, we analyse the azimuthal and axial symmetries of these terms, which are ultimately manifested in the streaming through the bubble boundary conditions (2.5) enforced at  $r=1$ . Let us consider the Reynolds stress term engendered by the product of two arbitrary oscillatory flow modes  $\mathbf{u}_0^{kl}$  and  $\mathbf{u}_0^{mn}$  of (3.2), defined by  $\boldsymbol{\sigma}^{kl,mn} = \langle \mathbf{u}_0^{mn} \cdot \nabla \mathbf{u}_0^{kl} + \mathbf{u}_0^{kl} \cdot \nabla \mathbf{u}_0^{mn} \rangle$ . Outside steady boundary layers, we have

$$\begin{aligned} \boldsymbol{\sigma}^{kl,mn} &= \frac{A_{mn}^* A_{kl}}{8nl\alpha^2 K'_{2m}(2n\alpha) K'_{2k}(2l\alpha)} \nabla (\nabla \varphi_{mn} \cdot \nabla \varphi_{kl}) \\ &= \frac{A_{mn}^* A_{kl}}{8nl\alpha^2 K'_{2m}(2n\alpha) K'_{2k}(2l\alpha)} \nabla \sum_{i=1}^2 \sum_{j=1}^2 \lambda_{ij}^{kl,mn}(r) \cos[2(m+(-1)^i k)\theta] \\ &\quad \times \cos[2(n+(-1)^j l)\alpha z], \end{aligned} \tag{3.7}$$

where the asterisk denotes the complex conjugate and

$$\lambda_{ij}^{kl,mn} = \frac{1}{4} g'_{mn}(r) g'_{kl}(r) - [(-1)^i m k + (-1)^j \alpha^2 n l] g_{mn}(r) g_{kl}(r), \tag{3.8}$$

with  $g_{mn}(r) \equiv K_{2m}(2\alpha nr)$ . The same azimuthal and axial symmetries also appear in analogous modes of the Stokes drift terms  $\mathbf{u}_d^{kl,mn}$  defined by

$$\mathbf{u}_d^{kl,mn} \equiv \left\langle \left( \int \mathbf{u}_0^{mn} dt \cdot \nabla \right) \mathbf{u}_0^{kl} + \left( \int \mathbf{u}_0^{kl} dt \cdot \nabla \right) \mathbf{u}_0^{mn} \right\rangle. \tag{3.9}$$

Through (2.3), these axial and azimuthal dependences of  $\sigma^{kl,mn}$  and  $\mathbf{u}_d^{kl,mn}$  are reflected directly in the steady outer solution (see e.g. Wang 1968; Davidson & Riley 1971; Longuet-Higgins 1998).

To first approximation, due to their large amplitudes, products of planar modes ( $n = 0$ ) contribute most strongly to (3.7), driving two-dimensional flow. Non-trivial axial dependences of  $\sigma$  arise predominantly from the product of the most strongly excited axial mode  $m = 0, n = 1$  (oscillating axisymmetric quadrupole) with the dominant two-dimensional mode  $k = l = 0$  (oscillating line source). The resulting forcing  $\sigma^{00,01}$ , by (3.7), is axisymmetric, with an axial wavelength equal to the channel depth  $d$ , forming the most strongly excited mode of the forcing term  $\sigma$ . Decomposed into its components in cylindrical coordinates, and neglecting higher-order mode combinations,  $\sigma$  therefore takes the approximate form

$$\sigma \approx \sigma^{00,01} = A_{00}A_{01}^* \{ \sigma_r(r) \cos 2\alpha z, 0, \sigma_z(r) \sin 2\alpha z \}, \tag{3.10}$$

where  $\sigma_r(r)$  and  $\sigma_z(r)$  are determined by the oscillatory flow functions. Note also that retaining the same axial modes (0, 1), but including higher-order planar modes ( $k > 0, l = 0$ ) results in Reynolds stresses with both axial and azimuthal variation. Reynolds stress terms quadratic in axial mode amplitudes, as well as contributions involving higher-order axial modes, are subdominant due to their weak excitation and will be ignored here. As we shall show presently, flows excited due to these modes are further suppressed by their strong radial decay away from the bubble surface.

### 3.1. Separable Stokes solutions

Motivated by the axial and azimuthal symmetries of the Reynolds stresses at the bubble (3.7), we seek separable solutions of (2.3). In general, the velocity field  $\mathbf{v}$  may be decomposed into its irrotational (conservative) part  $\mathbf{v}^C$  and a rotational (non-conservative) part  $\mathbf{v}^N$  (Doinikov 1997; Doinikov & Bouakaz 2010). The irrotational part of the flow has a form similar to (3.2) and is expressible in terms of the cylindrical harmonics  $\varphi_{mn}$  given by (3.3), allowing  $\mathbf{v}_{mn}^C \equiv \nabla \varphi_{mn}$  to satisfy the kinematic condition at all solid walls, but not at the bubble. For completeness, we give the expression for the components of  $\mathbf{v}_{mn}^C$  in cylindrical coordinates  $(r, \theta, z)$ :

$$\mathbf{v}_{mn}^C = \{ u_{mn}^C(r) \cos 2m\theta \cos 2n\alpha z, v_{mn}^C(r) \sin 2m\theta \cos 2n\alpha z, w_{mn}^C(r) \cos 2m\theta \sin 2n\alpha z \}, \tag{3.11}$$

where

$$\left. \begin{aligned} u_{mn}^C(r) &= -\frac{2n\alpha}{2} (K_{2m+1}(2n\alpha r) + K_{2m-1}(2n\alpha r)) \\ v_{mn}^C(r) &= -\frac{2m}{r} K_{2m}(2n\alpha r) \\ w_{mn}^C(r) &= -2n\alpha K_{2m}(2n\alpha r). \end{aligned} \right\} \tag{3.12}$$

The no-penetration condition at the bubble is satisfied by making use of the rotational, pressure-dependent solutions of the Stokes equations ( $\mathbf{v}^C$  is, by definition,

pressure independent). The effective pressure  $p$  itself is harmonic outside boundary layers ( $\nabla^2 p = 0$ ) due to (2.3), and may be decomposed into cylindrical harmonics (3.3). For the dimensionless pressure mode  $p_{mn} = \varphi_{mn}$ , rotational solutions  $\mathbf{v}_{mn}^N$  of the Stokes equations ( $\nabla^2 \mathbf{v}_{mn}^N = \nabla p_{mn}$ ) take the form

$$\mathbf{v}_{mn}^N = \{u_{mn}^N(r) \cos 2m\theta \cos 2n\alpha z, v_{mn}^N(r) \sin 2m\theta \cos 2n\alpha z, w_{mn}^N(r) \cos 2m\theta \sin 2n\alpha z\}, \tag{3.13}$$

where

$$\left. \begin{aligned} u_{mn}^N(r) &= -\frac{m}{2n\alpha} K_{2m+1}(2n\alpha r) + \frac{r}{2} K_{2m+2}(2n\alpha r) \\ v_{mn}^N(r) &= \frac{m+1}{2n\alpha} K_{2m+1}(2n\alpha r) \\ w_{mn}^N(r) &= \frac{r}{2} K_{2m+1}(2n\alpha r). \end{aligned} \right\} \tag{3.14}$$

Neglecting any axial Stokes drift contributions to the Lagrangian flow, the corresponding Lagrangian streaming mode  $\mathbf{v}_{mn}$  that satisfies the no-penetration condition at the interface  $r = 1$  and at the walls  $\partial\Omega_w$ , normalized to have unit peak axial velocity at  $\partial\Omega_b$ , may be written as

$$\mathbf{v}_{mn} = \left( \frac{w_{mn}^C(1)}{u_{mn}^C(1)} - \frac{w_{mn}^N(1)}{u_{mn}^N(1)} \right)^{-1} \left( \frac{\mathbf{v}_{mn}^C}{u_{mn}^C(1)} - \frac{\mathbf{v}_{mn}^N}{u_{mn}^N(1)} \right). \tag{3.15}$$

A general class of no-penetration Stokes solutions may be constructed using linear combinations of  $\mathbf{v}_{mn}$  (over  $m$  and  $n$ ), determined simultaneously by boundary conditions at the bubble and at the walls. Note, however, that  $\mathbf{v}_{mn}$  are characterized by exponential radial decays ( $\propto e^{-2n\alpha r}$ ). The dominance of the lowest axial mode in the Reynolds stress, together with the exponential radial decays of (3.15) into the fluid away from the bubble surface, ensures that the lowest (non-trivial) axial modes are both (i) the most strongly forced, and (ii) the predominant axial streaming solutions in the bulk of the flow. It is therefore appropriate to consider only the lowest axial modes ( $n = 1$ ) of (3.15), so that

$$\mathbf{v} \approx \sum_{m=0}^{\infty} c_{m1} \mathbf{v}_{m1}, \tag{3.16}$$

where the  $c_{m1}$  are determined by the slip condition (3.6) at the top and bottom wall. Since (3.16) is only a truncated representation of the flow, rather than satisfying the slip condition rigorously for all  $r > 1$ , we will focus on satisfying it only at  $r = 1$ . This is an appropriate simplification since the axial solutions presented here modify the flow significantly only near  $\partial\Omega_b$ , where the slip at walls due to the planar solution  $\mathbf{u}$  is the greatest (Rallabandi *et al.* 2014). At  $r = 1$ , the slip condition (3.6), along with (3.16) when decomposed into a Fourier series in  $\theta$ , yields the coefficients

$$c_{m1} = -\frac{\int_0^\pi \mathbf{u}(1, \theta) \cdot \hat{\boldsymbol{\theta}} \sin 2m\theta \, d\theta}{\int_0^\pi \mathbf{v}(1, \theta, d/2) \cdot \hat{\boldsymbol{\theta}} \sin 2m\theta \, d\theta}, \tag{3.17}$$

where  $\hat{\boldsymbol{\theta}}$  is the unit vector in the azimuthal direction.



Note that (3.17) does not determine the strength of the axisymmetric solution  $c_{01}$ , since (3.17) is specifically a statement of vanishing azimuthal velocity at the interface. It should be expected, however, that such a flow component is in general excited, in particular due to bubble oscillations that set up axisymmetric Reynolds stresses (3.10). The structure of the axisymmetric flows  $(r, z)$  is entirely analogous to planar flows  $(r, \theta)$  in the  $x$ - $y$  plane with respect to the governing equations and boundary conditions, albeit weaker in overall magnitude due to weaker forcing (smaller axial oscillation amplitudes). This suggests that the axisymmetric solution also inherits the ‘fountain’ structure of the two-dimensional solution due to the pinning of contact lines at the top and bottom walls (see e.g. Wang *et al.* 2013; Rallabandi *et al.* 2014), with radially outward velocities at the mid-plane ( $z=0$ ) and radially inward velocities near the top and bottom walls (cf. figure 2*b,c*).

In principle  $c_{01}$  may be evaluated from a detailed calculation of the Reynolds stresses. This however requires both (i) a resolution of the axial oscillation mode amplitudes  $A_{mn}$  as functions of frequency (see e.g. Gelderblom *et al.* 2012; Wang *et al.* 2013), and (ii) a detailed description of both oscillatory and steady no-stress boundary layers due to these flow modes, accurate up to  $O(\delta^2)$  (see e.g. Davidson & Riley 1971; Longuet-Higgins 1998; Rallabandi *et al.* 2014). We do not attempt to carry out this analysis rigorously here, but rather estimate  $c_{01}$  by considering the ratio between the damping coefficient  $\gamma_{00}$  of the monopole ( $m=0, n=0$ ) and that of the lowest axial mode ( $m=0, n=1$ ), denoted by  $\gamma_{01}$ ; cf. equation (21) of Wang *et al.* (2013). In the limit of small damping, the relative mode amplitude scales inversely with the relative damping coefficient; for the channel aspect ratio used in the present experiments ( $d/a=2.5$ ), this results in  $|A_{01}|/|A_{00}| \approx \gamma_{00}/\gamma_{01} \approx 0.32$ . Under the present normalization ( $|A_{00}|=1$ ), the velocity scale due to the product of the monopole and the axisymmetric quadrupole is therefore  $\sim 0.32u_s$ , resulting in  $|c_{01}| \sim 0.32$ . The value of  $c_{01}$  inferred from experimental measurements, described in more detail in §5, agrees closely with this estimate.

For  $m \geq 1$ , the coefficients  $c_{m1}$  may be computed directly from the two-dimensional theory, using (3.17). The ‘fountain’ structure of the planar flow  $\mathbf{u}$  (one vortex per quadrant, cf. figure 2*b*), naturally leads by (3.17) to  $|c_{11}| \gg |c_{m1}|$  for  $m > 1$ . Retaining therefore only terms of (3.16) proportional to  $c_{01}$  and  $c_{11}$ , the leading contributions to the three-dimensional streaming flow may be written as

$$\mathbf{U} = \mathbf{u} + c_{01}\mathbf{v}_{01} + c_{11}\mathbf{v}_{11} \quad (\mathbf{v} = c_{01}\mathbf{v}_{01} + c_{11}\mathbf{v}_{11}). \quad (3.18)$$

The two axial contributions  $c_{01}\mathbf{v}_{01}$  and  $c_{11}\mathbf{v}_{11}$  represent, respectively, the lowest axisymmetric and axial–azimuthal modes, and are depicted in figure 2(*a*). These contributions address, respectively, the excitation of steady flow due to axial bubble oscillations (axial oscillatory flow gradients) and the observance of no-slip conditions at axially confining walls.

#### 4. Results and discussion

Before we discuss the resultant flow  $\mathbf{U}$  in detail, it will prove useful to write the planar flow  $\mathbf{u} = \{u_r, u_\theta, 0\}$  in terms of a stream function  $\psi(r, \theta)$  so that  $u_r = r^{-1}\partial_\theta\psi$  and  $u_\theta = -\partial_r\psi$ . The steady two-dimensional flow is in general composed of a dominant fountain vortex and a sub-dominant anti-fountain vortex near the wall at  $y=0$  (Wang *et al.* 2013; Rallabandi *et al.* 2014). Here, we neglect the effect of the anti-fountain near the wall, which is typically confined to a region comparable in extent to the boundary layer thickness  $\delta$ , and is therefore greatly suppressed

by the (no-slip) wall boundary layer structure. The stream function  $\psi$  describing the two-dimensional Lagrangian streaming flow in a channel of finite height  $h$  is in general obtained by a modification of the solution obtained in the half-space ( $h \rightarrow \infty$ ), by the procedure outlined in appendix A. Focusing on the quadrant ( $x > 0, y > 0$ ), the two-dimensional steady flow is characterized by a single vortex system (closed streamlines) governed by  $\psi \in (\psi_m, 0)$ , where  $\psi = 0$  delineates the boundaries of the domain (largest enclosed area), and  $\psi = \psi_m < 0$  identifies the two-dimensional vortex centre (vanishing enclosed area, see figure 2*b*). The fountain vortex flow of figure 2*b*), with its outward flow near the symmetry plane  $\theta = \pi/2$  (Wang *et al.* 2012, 2013; Rallabandi *et al.* 2014) has a simple far-field approximation to the stream function for large channel height ( $h \rightarrow \infty$ ), namely,

$$\psi \sim \frac{4e_1}{r} \sin^2 \theta \cos \theta, \quad \text{as } r \rightarrow \infty, \tag{4.1}$$

where  $e_1$  is an  $O(1)$  constant related to planar oscillation mode amplitudes and phases and is negative for fountain-mode streaming (Rallabandi *et al.* 2014).

The superposition of the two-dimensional Lagrangian streaming with the flows computed in the previous section yields a three-dimensional steady flow that satisfies (i) the Stokes equations, (ii) no-penetration conditions at all boundaries and (iii) no-slip conditions at the confining walls close to the interface. We will focus on material trajectories in this flow, given by solutions  $\mathbf{x}(t)$  of  $\dot{\mathbf{x}}(t) = \mathbf{U}(\mathbf{x}(t))$ , which are integrated numerically using a fourth-order Runge–Kutta scheme. Due to the symmetry of the problem, we focus our results on the region  $x > 0, 0 < y < h, 0 < z < d/2$ . The smallest time scale relevant to the steady flow is the time scale of fluid advection along the bubble interface, which we define as  $T_s \equiv a/u_s = 1/(\epsilon^2\omega)$ , and use to non-dimensionalize time for all the results following below.

The two-dimensional vortex motion occurs over the nominal orbit time along closed two-dimensional streamlines (under the action of  $\mathbf{u}$  alone), which is much greater than  $T_s$  due to the algebraic decay of the flow velocity away from the bubble. In units of  $T_s$ , the dimensionless planar orbit time on a streamline  $T(\psi)$  is in general defined by

$$T(\psi) = \oint_{\psi} \frac{1}{|\mathbf{u}|} ds = \oint_{\psi} \frac{1}{|\nabla\psi|} ds, \tag{4.2}$$

where  $ds = |\mathbf{u}| dt$  is a differential arclength element along the streamline and the path of integration along  $\psi$  is counterclockwise. Using the far-field solution (4.1), one may estimate  $T(\psi)$  as

$$T_{h \rightarrow \infty}(\psi) \approx \int_{\pi/2}^0 \frac{r(\psi, \theta)}{u_{\theta}(\psi, \theta)} d\theta = -\frac{\pi e_1^2}{2\psi^3}. \tag{4.3}$$

This estimate, valid for  $h \rightarrow \infty$ , becomes quantitatively modified for flow fields with finite  $h$  (see appendix A), but the order of magnitude of  $T(\psi) \sim 10T_s - 100T_s$  obtained from (4.3) remains valid.

#### 4.1. Three-dimensional effects on short and long time scales

The axial flows modify the two-dimensional motion in at least two significant ways. Perhaps most strikingly, a fluid particle trajectory close to the bubble ( $r \lesssim 1 + d/(2\pi)$ ) shows strong bursts of axial displacement on the short time scale  $\sim T_s$ , much shorter

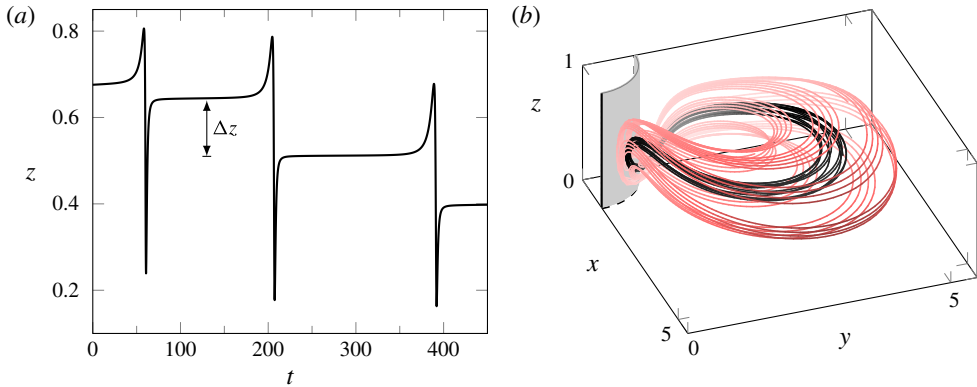


FIGURE 3. (Colour online) (a) Axial motion  $z(t)$  of a typical fluid particle trajectory, showing the strong bursts of axial displacement (when the trajectory is close to the bubble surface) and the net axial displacement  $\Delta z$  over one cycle of radial motion. (b) Fluid particle trajectories for two different initial conditions, showing the nested torus structure: light red is a trajectory of large axial extent, while black indicates a trajectory close to the ‘core’ of the torus. The solid black line at  $(x=1, y=0)$  indicates the bubble contact line with the bounding wall, dashed lines indicate the locations of symmetry planes intersecting the bubble surface at  $(z=0, r=1)$  and  $(x=0, y=1)$ .

than the two-dimensional orbit time. Figure 3(a) shows an example of such a trajectory: as axial flow components of  $\mathbf{v}$  very close to the bubble are in general comparable to planar velocity components due to the coupling (3.6), the fluid element approaches the bubble and is advected along the interface (in the direction  $\theta \rightarrow \pi/2$ ), suffering  $O(1)$  axial displacements over the time scale  $T_s$ . The axial confinement necessitates a spatial reversal of the axial velocity components, so that a fluid element experiences axial displacements both towards and away from the mid-plane during the course of its motion near the bubble. As a consequence, the net axial displacement ( $\Delta z$ ) of a fluid element over the intermediate time scales  $T(\psi)$ , averaged over its nominal two-dimensional orbit, is typically small compared to the bubble radius (figure 3a).

Figure 3(b) illustrates the long-time effect of these net displacements: similar to the axial  $\Delta z$ , planar components of  $\mathbf{v}$  result in small deviations of the planar projections of fluid trajectories from nominally closed two-dimensional orbits. If the depth of the channel is on the order of the bubble radius (or greater), the small axial and planar drifts result in a motion over time scales longer still than  $T(\psi)$ , over which a fluid element explores a significant fraction of the half-channel by systematically sampling a succession of planar orbits of varying planar extents (varying  $\psi$ ) at different depths  $z$  (cf. figure 8). The superimposed axial and radial motions result in quasi-periodic trajectories that fill toroidal structures in three dimensions (figure 3b). It can be seen that fluid elements at different initial positions follow toroidal trajectories of considerably varying spatial extents, none of which intersect. At the core of this nested system of tori is a singly periodic trajectory of vanishing toroidal volume.

The long-time toroidal motion of a fluid element is further illustrated in figure 4(a): its quasi-period  $\tau$  depends on the initial position of the fluid particle, with net motion towards the mid-plane  $z=0$  occurring over the widest planar orbits ( $\psi \sim 0$ ), followed by motion towards the wall ( $z=d/2$ ) occurring over ‘tight’ planar orbits that are

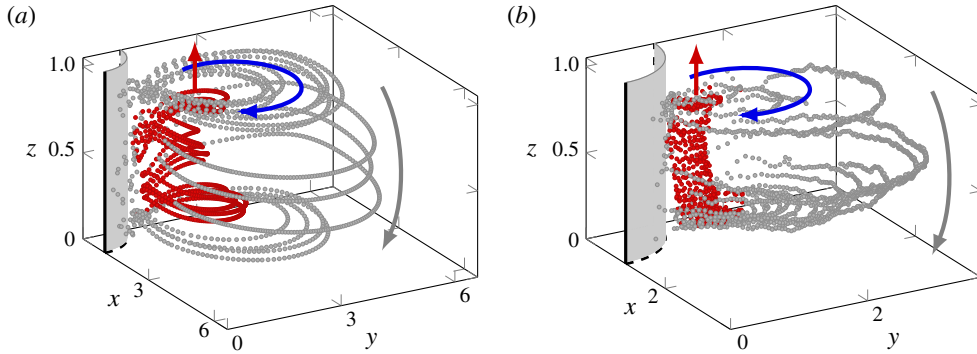


FIGURE 4. (Colour online) Typical toroidal trajectory, as (a) predicted by the theory for a fluid element, and (b) measured experimentally for an approximately passive tracer by APTV, cf. Marin *et al.* (2015). The motion is towards the channel walls on the tight orbits (close to the nominal two-dimensional vortex centre), indicated in red, and towards the channel mid-plane during wider planar orbits, coloured grey. Arrows indicate these axial motions as well as the two-dimensional fountain orientation (blue).

closer to the two-dimensional vortex centre ( $\psi \sim \psi_m$ ). Reversals in the direction of the slow axial motion occur near the wall and the mid-plane, involving relatively large changes in the planar extent of the quasi-planar orbits, i.e. a widening of tight orbits near the wall, and a tightening of wide orbits close to the mid-plane (see figure 4). As discussed in § 5, all elements of this motion are observed in experiment as well (figure 4b).

#### 4.2. Generalized Hamiltonian theory of three-dimensional effects

The wide spatial range explored by different material points underscores the importance of understanding the kinematics of these trajectories, particularly in the context of applications such as fluid mixing and manipulation of microparticles in these flows.

By definition, the displacement in the  $z$  coordinate of a fluid element is simply the time integral of the axial component of the velocity field as a function of its instantaneous position  $\mathbf{x}(t)$ . However, the drift in the  $z$  coordinate of a fluid element over a time  $T(\psi)$ , denoted by  $\Delta z$ , is typically much smaller than the channel depth  $d$  (see figure 3a), with significant axial motion only occurring over much longer time scales. In the limit  $\Delta z/d \ll 1$  (or otherwise  $|\mathbf{v}| \ll |\mathbf{u}|$ ), the motion of the particle over a time  $T(\psi)$  is therefore approximately planar to leading order in  $\Delta z$ , i.e.  $\mathbf{x}(t) \approx \tilde{\mathbf{x}}(t) = \{r(t), \theta(t), z\}$  such that  $z$  and  $\psi = \psi(r(t), \theta(t))$  are approximately constant over the motion. For  $\Delta z/d \ll 1$ , one may therefore compute  $\Delta z$  as the integral axial displacement of a fluid element as it traverses a nominally closed two-dimensional orbit (constant  $z$  and  $\psi$ ), over the time  $T(\psi)$ . To first approximation, we may write

$$\Delta z(\psi, z) = \int_0^{T(\psi)} v_z(\mathbf{x}(t)) dt \approx \int_0^{T(\psi)} v_z(\tilde{\mathbf{x}}(t)) dt. \quad (4.4)$$

Note that the absolute values of the limits in the time integral are unimportant as long as their difference is  $T(\psi)$  – this ensures an integral over the entire closed orbit  $\psi$ , valid for all material points on  $\psi$ . The  $\Delta z$  defined by (4.4) therefore represents the deviation of a material orbit from planarity over the time  $T(\psi)$ .

The deviation from closedness of orbits over a time  $T(\psi)$ , when projected on the  $x$ - $y$  plane, may be similarly quantified by a drift in  $\psi$  (denoted by  $\Delta\psi$ ) of a fluid element. The time rate of change of the stream function value  $\psi$  sampled by a fluid element as it is advected by the three-dimensional flow field  $\mathbf{U}$  is simply the material derivative of  $\psi$ , which for steady flow is given by  $\mathbf{U} \cdot \nabla\psi = \mathbf{v} \cdot \nabla\psi$ . If we again assume small deviations from closedness over a planar orbit time scale,  $\Delta\psi$  over the time  $T(\psi)$  is computed to first approximation as

$$\Delta\psi(\psi, z) = \int_0^{T(\psi)} \mathbf{v}(\mathbf{x}(t)) \cdot \nabla\psi(\mathbf{x}(t)) dt \approx \int_0^{T(\psi)} \mathbf{v}(\tilde{\mathbf{x}}(t)) \cdot \nabla\psi(\tilde{\mathbf{x}}(t)) dt. \tag{4.5}$$

It may be shown (see appendix B) that for an arbitrary incompressible velocity field  $\mathbf{v}$ , the approximate drifts  $\Delta z$  and  $\Delta\psi$  (using  $\tilde{\mathbf{x}}(t)$ ) defined respectively by (4.4) and (4.5), identically satisfy the differential continuity equation

$$\frac{\partial \Delta\psi}{\partial \psi} + \frac{\partial \Delta z}{\partial z} = 0. \tag{4.6}$$

This automatically allows them to be expressed in terms of a Hamiltonian  $\mathcal{H}(\psi, z)$  as

$$\Delta\psi = \frac{\partial \mathcal{H}}{\partial z}, \quad \Delta z = -\frac{\partial \mathcal{H}}{\partial \psi}, \tag{4.7a,b}$$

where  $\mathcal{H}(\psi, z)$  may be written as

$$\mathcal{H}(\psi, z) \equiv - \int \oint_{\psi} \mathbf{v} \cdot \mathbf{n} ds dz, \tag{4.8}$$

and  $\mathbf{n} \equiv -\nabla\psi/|\nabla\psi|$  is the local unit normal to streamlines in the  $x$ - $y$  plane; see appendix B for a more detailed discussion. Since these drifts occur over a planar orbit time  $T(\psi)$ , one may define mean drift velocities as

$$\bar{v}_{\psi}(\psi, z) \equiv \frac{1}{T} \frac{\partial \mathcal{H}}{\partial z}, \quad \bar{v}_z(\psi, z) \equiv -\frac{1}{T} \frac{\partial \mathcal{H}}{\partial \psi}. \tag{4.9a,b}$$

The system (4.9) constitutes precisely an incompressible two-dimensional flow field in the abstract  $\psi$ - $z$  space, governed by the Hamiltonian  $\mathcal{H}(\psi, z)$ , which plays the role of a stream function and remains invariant over the long-time three-dimensional steady motion of a fluid element. Since both  $\mathbf{u}$  and  $\mathbf{v}$  involve vanishing normal velocities on  $\partial\Omega$ , it follows from (4.8) and (4.9) that the flow in the abstract space does not penetrate its boundaries, i.e.

$$\bar{v}_{\psi}(\psi_m, z) = \bar{v}_{\psi}(0, z) = \bar{v}_z(\psi, 0) = \bar{v}_z(\psi, d/2) = 0. \tag{4.10}$$

This automatically ensures the existence of at least one elliptic point  $(\psi_c, z_c)$  at which  $\partial_{\psi}\mathcal{H} = \partial_z\mathcal{H} = 0$ , which represents a two-dimensional curve in real space given by  $\psi(r, \theta) = \psi_c, z = z_c$ . Any material point on this curve, by virtue of lying on a (stable) stagnation point of the  $\psi$ - $z$  flow, remains confined to it under the action of the three-dimensional flow field, i.e. the curve in real space defined by  $(\psi_c, z_c)$  approximates the core of the system of nested toroidal fluid trajectories (cf. figure 3b). Curves of constant  $\mathcal{H}$  in the vicinity of the core are concentric about it, spanning

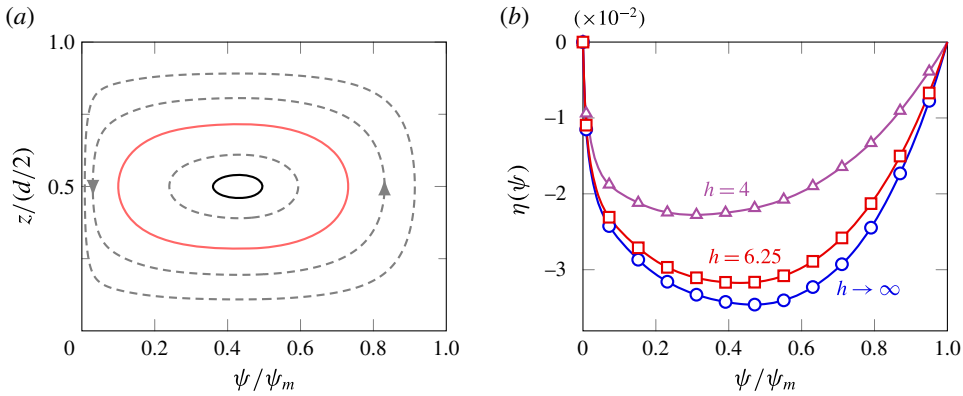


FIGURE 5. (Colour online) (a) Phase portrait of the Hamiltonian system in  $\psi$ - $z$  space, computed for  $h \rightarrow \infty$ . Closed dashed lines are curves of constant  $\mathcal{H}$  representing three-dimensional tori in real space, with the light red and black solid-line trajectories corresponding to the respective tori in figure 3(b). (b) Functions  $\eta(\psi)$  at  $f = 20$  kHz and  $d = 2.5$  for different channel heights  $h$ .

finite ranges of axial coordinates  $z$  and streamlines  $\psi$ , and therefore delineate surfaces of the tori on which fluid elements move in real space. Figure 5(a) shows the  $\psi$ - $z$  phase portrait that provides this simplified description of the three-dimensional motion. It is noteworthy that this description assumes no particular forms for  $u$  and  $v$ , only requiring that the two-dimensional flow is steady and characterized by closed streamlines, and is therefore in principle applicable to any perturbed two-dimensional flow under confinement.

For  $v$  given by (3.18) (single axial wavenumber), the Hamiltonian is separable and takes the form

$$\mathcal{H} = \eta(\psi) \sin 2\alpha z, \tag{4.11}$$

so that

$$\bar{v}_\psi = \frac{2\alpha}{T(\psi)} \eta(\psi) \cos 2\alpha z, \quad \bar{v}_z = -\frac{1}{T(\psi)} \eta'(\psi) \sin 2\alpha z. \tag{4.12a,b}$$

The core trajectory is therefore located at  $z_c = d/4$  and  $\eta'(\psi_c) = 0$ ; note that  $\eta'(\psi)$  is guaranteed to have at least one zero within the relevant range of stream function values  $(\psi_m, 0)$ . The temporal evolution of the stream function is therefore given by

$$\frac{d\psi}{dt} = \pm \frac{2\alpha}{T(\psi)} \sqrt{\eta^2 - \mathcal{H}^2}. \tag{4.13}$$

The characteristic function  $\eta(\psi)$  itself is obtained from evaluating (4.8) and (4.11), and displayed in figure 5(b). Its shape is relatively insensitive to the channel width for  $h$  not too small.

Equation (4.13) may be solved numerically for given initial conditions  $(z_0, \psi_0)$ . For trajectories that approach the core,  $\mathcal{H} \sim \mathcal{H}(\psi_c, z_c)$ , orbits in the  $\psi$ - $z$  plane are elliptical so that  $\psi(t)$  and  $z(t)$  both vary sinusoidally with a single frequency. For arbitrary  $\mathcal{H}$ , the temporal motion is asymmetric over a three-dimensional period  $\tau$  due to the dependence of the drift velocities on  $1/T(\psi)$ , so that the axial dynamics are faster for smaller orbits  $\psi/\psi_m \sim 1$ , and slower for larger planar orbits  $\psi/\psi_m \sim 0$ .

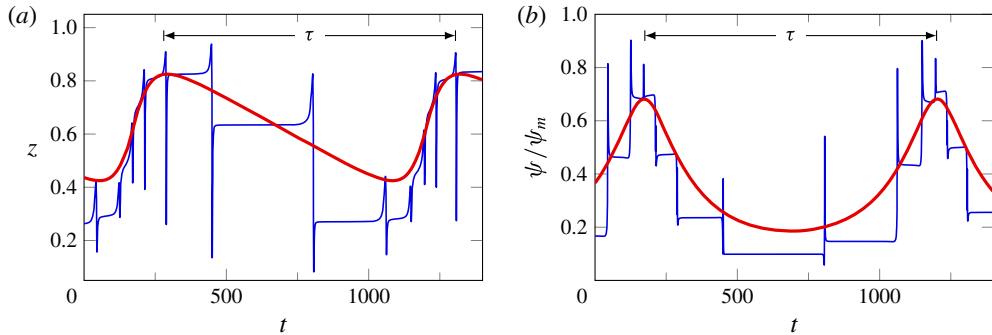


FIGURE 6. (Colour online) (a) Axial coordinate  $z$  and (b) normalized stream function  $\psi/\psi_m$  as functions of time, over approximately one three-dimensional quasi-period  $\tau$ . Blue lines represent the numerical integration of particle trajectories, while red lines show the predictions of the Hamiltonian theory, which captures the long-time kinematics while averaging over the shorter time scales.

In real space, this corresponds to the faster axial motion towards the top wall ( $z=d/2$ ) over tight planar orbits, and the slower axial drift towards the mid-plane ( $z=0$ ) over wider orbits, as depicted in figure 6(a), where the red line indicating the Hamiltonian theory captures the asymmetry of the long-time motion. The  $\psi$ -motion depicted in figure 6(b) is much more symmetric, but is also subject to abrupt jumps on the short time scale.

### 5. Experimental data for three-dimensional streaming flows

A microbubble streaming set-up of the type depicted in figure 1(a) was used to obtain three-dimensional trajectory data for approximately passive tracer particles (polystyrene beads of diameter  $2\ \mu\text{m}$ ) utilizing APTV (Cierpka *et al.* 2011; Cierpka & Kähler 2012; Rossi & Kähler 2014). In this optical imaging technique, the image of a spherical tracer particle is distorted by a cylindrical lens into elliptic shapes whose eccentricity depends on the depth coordinate of the particle along the optical axis. This allows the quantification of all three velocity components of moving tracer particles in a three-dimensional domain with a single camera. The experiments were conducted using  $a = 40\ \mu\text{m}$ ,  $f = 20\ \text{kHz}$ ,  $d = 2.5$ , and  $h = 25$ , with particle images taken by a high-speed camera connected to an inverted microscope, at a recording speed of 500 f.p.s. The measurement uncertainty of this technique arises primarily from errors in particle detection and tracking, and the degree to which the elliptical shapes of the particle images can be accurately determined (see Rossi & Kähler 2014 for details). For the present experiments, the measurement uncertainty in the position of a particle is  $\approx \pm 0.1\ \mu\text{m}$  in the  $x$  and  $y$  directions and  $\approx \pm 1\ \mu\text{m}$  in the  $z$  direction, much smaller than typical length scales of interest ( $\sim 10\ \mu\text{m}$ ). More details about this use of the technique in a microfluidic context and more experimental data on bubble microstreaming are presented in Marin *et al.* (2015). Figure 4(b) displays an example trajectory that shows all the qualitative features predicted by the three-dimensional streaming theory: one trajectory typically occupies half the channel (between one wall and the mid-plane) and consists of approximately two-dimensional trajectory loops whose radial extent is small as the particle is displaced towards the wall, then widens to a greater radial extent as the  $z$ -motion reverses and the particle moves towards the mid-plane.

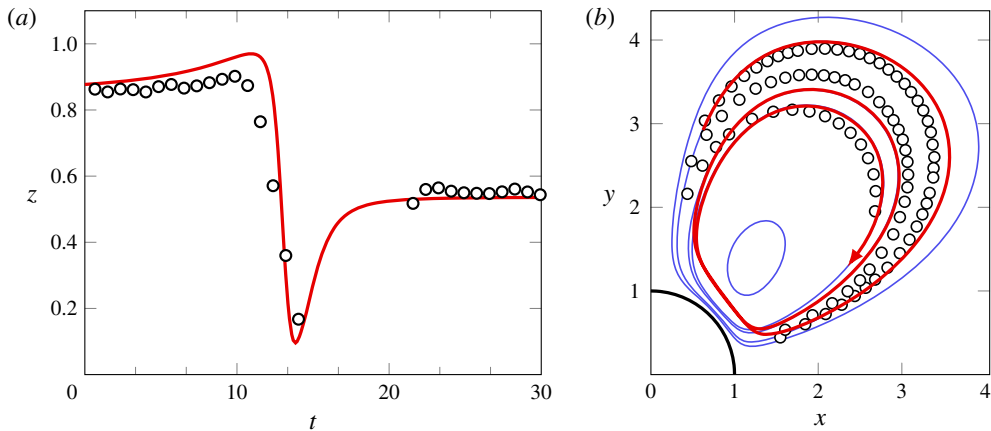


FIGURE 7. (Colour online) (a) Axial motion of a particle over short time scales in the vicinity of the bubble, predicted by the theory (solid line) and measured experimentally (markers). Note the large  $O(1)$  axial excursion of the particle on the shortest time scales  $\sim T_s$  as it passes close to the bubble, which ultimately results in a smaller net axial displacement  $\Delta z$ , informing the long-time three-dimensional motion. (b) Projection of a part of a three-dimensional particle trajectory in the  $x$ - $y$  plane computed from  $\mathbf{U}$  (red), showing the radial drift as a systematic spiralling deviating from the two-dimensional periodic orbits (blue), with deviations concentrated at locations close to the bubble surface.

In order to model the axial motion quantitatively, we obtain the value of  $c_{01}$  from the experimentally measured azimuthal profile of the axial velocity component  $U_z(\theta)$  near the bubble ( $r \approx 1$ ), which determines the ratio  $c_{01}/c_{11}$ . This yields  $c_{01}$ , since  $c_{11} \approx -1.41$  is given automatically by (3.17) and the theoretical  $\mathbf{u}$ , thereby fixing the shape of the flow. The value of  $c_{01} \approx -0.34$  obtained by this procedure confirms that the axisymmetric component flow in the experiment (i) has the ‘fountain’ orientation ( $c_{01} < 0$ ) and (ii) is weaker than the planar component, with a magnitude that agrees well with the theoretical estimate (using damping coefficients) of  $|c_{01}| \sim 0.32$  (cf. § 3). In order to non-dimensionalize the experimental times, we first extrapolate the experimentally measured velocity onto the bubble surface, which yields a maximum slip velocity  $u_{max}$  at the interface, which is then translated into an experimental oscillation amplitude  $\epsilon$  using the prediction (from two-dimensional theory) of  $u_{max}/(\epsilon^2 a \omega) \approx 1.54$ . The computed value of  $\epsilon$  determines the time scale  $T_s = 1/(\epsilon^2 \omega)$ , which is used to scale time in the experiments for a comparison with theory. It should be stressed that, therefore, all theoretical figures and computations in the present work (unless explicitly stated otherwise) directly use parameters employed in practical bubble microstreaming experiments:  $d = 2.5$ ,  $h = 6.25$  for the channel geometry,  $a = 40 \mu\text{m}$ ,  $f = 20 \text{ kHz}$ , and the appropriate  $c_{01}$  inferred above.

We show here that the experiment confirms the theoretical results on all three distinct time scales: (i) the fast time scale  $\sim T_s$  of strong axial displacement; (ii) the intermediate time scale  $\sim 10T_s$ – $100T_s$  of the approximately two-dimensional vortex motion; and (iii) the very long time scale  $\tau \sim 1000T_s$  involving the toroidal motion with systematic variation of the axial position of the particle, accompanied by a slow variation of the extent of the planar motion. Figure 7(a) demonstrates that the strong, fast displacements along the  $z$ -axis are temporally resolved in experiments and in very good agreement with the theoretical prediction, including the characteristic



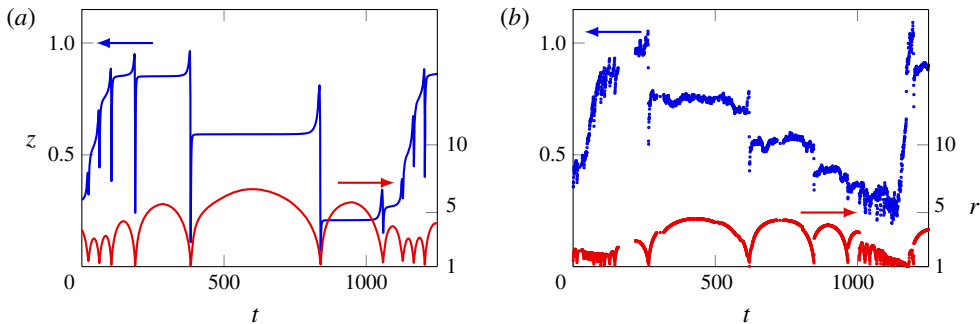


FIGURE 8. (Colour online) Axial and radial positions of a fluid element determined by numerical integration (a) and of an approximately passive tracer in experiment (b). Both show that the long-time three-dimensional motion is organized into simpler two-dimensional orbits (constant  $z$ ). The slow axial motion is towards the wall  $z = d/2$  on tight orbits (small maximum  $r$  in regions of constant  $z$ ) and in the opposite direction for wide orbits (large maximum  $r$  in regions of constant  $z$ ), quantifying the toroidal motion seen in figure 4(b).

asymmetry between the positive and negative portions of the  $z$ -displacement motion, which ultimately leads to the drifts  $\Delta z$ . Figure 7(b) shows that the motion projected into the  $x$ - $y$  plane still reproduces the ‘typical’ two-dimensional fountain dynamics. Limitations in the experimental time resolution prevent us from verifying directly the predicted deviations of the projected three-dimensional trajectories (red) near the bubble from the streamlines resulting from the two-dimensional theory (blue). It is interesting to note, though, that the  $xy$ -projection of a tracer particle on such a trajectory shows a spiralling motion towards the two-dimensional vortex centre, an observation commonly made in cylinder streaming (Lutz, Chen & Schwartz 2005; Lutz *et al.* 2006) and ascribed to inertial forces on the particles (as supported by numerical computations, cf. Chong *et al.* 2013). Finally, figure 8 confirms that the pattern of motion over long time scales  $\tau \sim 1000T_s$  is also modelled successfully: both the pattern of slow displacement along the  $z$ -axis and the pattern of widening and tightening radial extent of trajectories are confirmed in experiments, as is the strong correlation between the two motion patterns. Figure 8 thus allows a quantitative verification of the toroidal motion pattern of figure 4(b).

Prior to these new APTV experiments, there has only been one report of three-dimensional boundary streaming flow, for a cylinder oscillated along a diameter (Lutz *et al.* 2005), cf. figure 9(a). The patterns of streaming along the cylinder axis show significant differences to the bubble streaming, but it must be realized that even a strictly two-dimensional theory of cylinder streaming (Holtmark *et al.* 1954; Wang 1968; Bertelsen, Svardal & Tjøtta 1973) reveals very different patterns from two-dimensional bubble streaming. In particular, a ‘DC boundary layer’ is typically present, i.e. every quadrant of the streaming flow in the  $x$ - $y$  plane has two radially stacked vortices. Thanks to the general nature of our approach to describing three-dimensional flows as a perturbation of the two-dimensional patterns, however, it is possible to obtain a three-dimensional solution for cylinder streaming as well. This is helped by the absence of axial oscillations of the (solid) cylinder, so that  $c_{01}$  is identically zero. The only flow mode magnitude  $c_{11}$  is determined again by (3.17), with  $\mathbf{u}$  now representing the steady streaming flow outside the no-slip cylinder boundary layer, as given by a leading-order expansion in powers of  $\delta$  of the solution derived by Bertelsen *et al.* (1973).

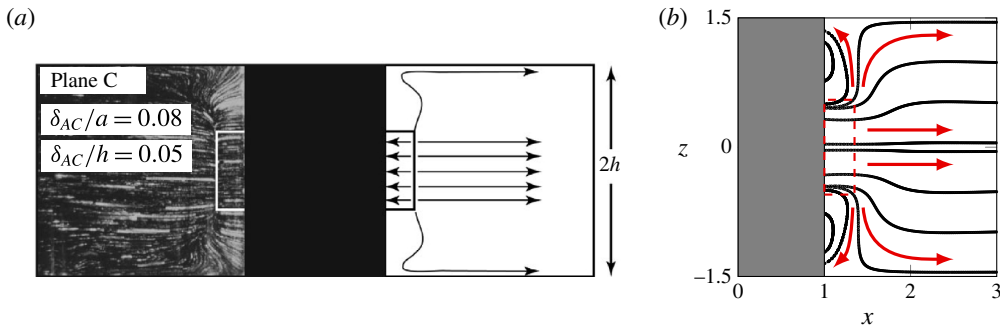


FIGURE 9. (Colour online) (a) Fluid trajectories under three-dimensional streaming due to an oscillating solid cylinder under axial confinement, projected in a plane containing the cylinder axis  $z$  and the axis of oscillation  $x$ . The right-hand part of the figure sketches the direction of motion of some tracer particles (reprinted with permission from Lutz *et al.* (2005), AIP Publishing LLC). (b) Analogous figure utilizing the present theory, showing qualitative agreement with the flow directions and the flow organization, including the ‘DC boundary layer’ region indicated by boxed outlines in experiment and theory. The length of the cylinder axis relative to its radius in both the experimental image of Lutz *et al.* (2005) and the present theory is  $d = 3$ .

The qualitative experimental image of figure 9(a) from Lutz *et al.* (2005) does not contain three-dimensional information, but is a projection with finite depth of field showing multiple flow lines. Likewise, figure 9(b) shows characteristic flow lines projected onto the  $x-z$  plane ( $x$  being the axis of oscillation of the cylinder), the same plane as in figure 9(a). Streamlines point away from the bubble and towards the walls outside the nominal ‘DC boundary layer’, whose radial extent is marked by the ‘box’ outlines in the experimental and theoretical figures. Close to the mid-plane, the flow appears two-dimensional, with axial motion being restricted to regions close to the wall; these flow features are in qualitative agreement with the results of Lutz *et al.* (2005) and demonstrate the wider applicability of our formalism to three-dimensional streaming flows.

## 6. Conclusions

We have developed the first description of three-dimensional boundary streaming flow patterns by employing a perturbation approach to microbubble streaming of planar symmetry. We found that the requirement of no-slip boundary conditions at the top and bottom walls (where the axis of the cylindrical bubble ends), as well as the presence of axial oscillations on the bubble surface, cause steady streaming modes that break the cylindrical symmetry, but do so in a very systematic fashion: axisymmetric modes are excited by axial bubble oscillations, while higher azimuthal modes are excited to satisfy no-slip conditions at the top/bottom walls. These flow contributions modify the two-dimensional trajectories in distinctive ways and on different time scales: while the flow remains two-dimensional to very good approximation over times comparable to the orbit time of this idealized two-dimensional motion, tracer particles experience (i) strong axial excursions over short time scales, when they are in the vicinity of the bubble surface, and (ii) systematic small radial and axial displacements over long times, which give rise to a longer-time periodicity of motion, in which the particles follow quasi-periodic orbits on a toroidal surface. All of these features are observed and confirmed in quantitative APTV experiments.

The long-time motion allows an analytical description as a Hamiltonian flow in an abstract space, giving a reduced-order description of the flow in the spirit of a time-scale separation. The very general character of this approach should make it applicable to a large class of confined Stokes flow problems where the three-dimensionality of the confinement interferes with an original greater symmetry of the imposed flow. The formalism has shown its merits by comparison with streaming from a solid cylinder.

The three-dimensional flow effects in bubble streaming discussed here have important implications for applications of this microstreaming technique. In micro-mixing set-ups using such bubbles (Liu *et al.* 2002; Ahmed *et al.* 2009; Wang *et al.* 2013; Rallabandi *et al.* 2015) the basic two-dimensional character of the flow makes it difficult to achieve strong (exponential) mixing, necessitating specific protocols of unsteadiness. The presence of axial flow components, in particular when it can be enhanced over the case presented here, should help achieve mixing more efficiently and quickly. In applications of particle sorting (Wang *et al.* 2011, 2012; Thameem, Rallabandi & Hilgenfeldt 2015), selective displacement of particles by size is achieved close to the bubble over very short time scales – while the long-time motion of the three-dimensional trajectories is of no concern in this case, the axial displacements of particles near the bubble need to be figured into the description of the sorting phenomenon. Three-dimensional flow features could potentially be used to concentrate particles near the centre of the channel, and thus assist a sorting of greater selectivity. For a much wider range of microfluidics set-ups, the tools developed here will be helpful to assess, model, and either minimize or enhance three-dimensional flow effects that could be desirable or undesirable in numerous applications e.g. in the context of lab-on-a-chip, cell diagnostic, or microTAS devices.

### Acknowledgements

We thank C. Wang, J. Freund, and R. Thameem for helpful discussions. B.R. and S.H. acknowledge support by the National Science Foundation for this work under grant no. CBET-1236141. A.M. and M.R. are thankful for support by the Deutsche Forschungsgemeinschaft (DFG) under grants no. KA1808/12-1 and KA1808/13-1.

### Appendix A. Two-dimensional bubble streaming in a channel

We outline a method to modify the steady two-dimensional half-space streaming flow solution  $\psi$  given by Rallabandi *et al.* (2014) so as to incorporate a no-slip wall at  $y=h$ , while leaving boundary conditions at the bubble and the  $y=0$  wall undisturbed. We will employ the modification

$$\psi \mapsto \psi + \chi, \quad (\text{A } 1)$$

where  $\chi$  is a correction flow to account for finite  $h$ . If  $\psi$  already satisfies the appropriate boundary conditions at  $r=1$  and  $y=0$ , and  $\chi$  is a Stokes flow (neglecting boundary layer terms), we have (temporarily neglecting bubble boundary conditions)

$$\left. \begin{aligned} \nabla^4 \chi &= 0 && \text{in } \Omega \\ \partial_x \chi &= \partial_y \chi = 0, && \text{on } y = 0 \\ \partial_y \chi &= -\partial_y \psi \equiv u(x), && \text{on } y = h \\ \partial_x \chi &= -\partial_x \psi \equiv -v(x), && \text{on } y = h. \end{aligned} \right\} \quad (\text{A } 2)$$

Solutions to (A 2) can be obtained using a Fourier transform pair in  $x$  defined by

$$\hat{f}(k) = \int_{-\infty}^{\infty} f(x) e^{-ikx} dx, \quad f(x) = \frac{1}{2\pi} \int_{-\infty}^{\infty} \hat{f}(k) e^{ikx} dk. \quad (\text{A } 3a,b)$$

The solution to the Fourier transform of  $\chi$  is then

$$\hat{\chi}(k, y) = \hat{a} \cosh ky + \hat{b} \sinh ky + \hat{c}y \cosh ky + \hat{d}y \sinh ky, \quad k \neq 0, \tag{A 4}$$

where

$$\left. \begin{aligned} \hat{a} &= 0 \\ \hat{b} &= -\frac{2i \hat{v}kh \cosh kh + (i\hat{u}kh + \hat{v}) \sinh kh}{k(1 + 2k^2h^2 - \cosh 2kh)} \\ \hat{c} &= -\hat{b}k \\ \hat{d} &= 2\frac{\hat{u}kh \cosh kh - (\hat{u} + i\hat{v}kh) \sinh kh}{1 + 2k^2h^2 - \cosh 2kh}. \end{aligned} \right\} \tag{A 5}$$

The superposition  $\psi + \chi$  obeys both  $y = 0$  and  $y = h$  wall boundary conditions, but now ignores bubble boundary conditions, applying inhomogeneous normal velocities and tangential stresses at  $r = 1$ . These inhomogeneities are accommodated by a second complementary flow obtained by a combination of half-space no-slip Stokes solutions (see e.g. Rallabandi *et al.* 2014), which introduce new inhomogeneities at  $y = h$ . Iterative application of (i) Fourier analysis to satisfy boundary conditions at  $y = h$  and (ii) half-space no-slip solutions to satisfy bubble boundary conditions yields the appropriate two-dimensional streaming solution  $\psi$  for arbitrary  $h$ . For  $h \gtrsim 4$ , two of these iterations are sufficient to implement all boundary conditions to excellent accuracy.

**Appendix B. Proof of the continuity equation (4.6)**

We present here a proof of the continuity equation (4.6) in  $\psi$ - $z$  space, valid for small perturbations  $\mathbf{v}$  of an incompressible two-dimensional flow  $\mathbf{u}$  characterized by closed streamlines. This automatically yields the Hamiltonian structure of the three-dimensional motion (4.7), governed by the Hamiltonian  $\mathcal{H}(\psi, z)$  defined in (4.8).

Consider a two-dimensional vortex characterized by closed streamlines  $\psi$  about a vortex centre  $\psi = \psi_m$ . If  $\mathbf{v}$  only slightly perturbs the two-dimensional fluid motion due to  $\mathbf{u}$ , one may approximate fluid trajectories as being two-dimensional (constant  $\psi, z$ ) to leading order over short times, i.e.  $\mathbf{x}(t) \approx \tilde{\mathbf{x}}(t)$ , discussed in §4.2. It is useful under this approximation to define a differential arclength element  $ds = |\mathbf{u}| dt = |\nabla\psi| dt$ , and a local unit outward normal  $\mathbf{n}$ , given for counterclockwise flow by  $\mathbf{n} \equiv -\nabla\psi/|\nabla\psi|$ . To leading order, time integration over a two-dimensional orbit time  $T(\psi)$  may therefore be replaced by a path integral over a streamline  $\psi$ . Using definitions for  $ds$  and  $\mathbf{n}$  and the divergence theorem, (4.5) may be recast as

$$\Delta\psi(\psi, z) = -\int_0^{T(\psi)} \mathbf{v} \cdot \mathbf{n} |\nabla\psi| dt = -\oint_{\psi} \mathbf{v} \cdot \mathbf{n} ds = -\int_{A(\psi)} \nabla_2 \cdot \mathbf{v} dA, \tag{B 1}$$

where  $A(\psi)$  is the area enclosed by a streamline  $\psi$  and  $\nabla_2$  is the two-dimensional gradient operator in the  $x$ - $y$  plane. The differential area element may in general be written as

$$dA = ds(\mathbf{n} \cdot d\mathbf{x}). \tag{B 2}$$

For counterclockwise flow, the definitions for  $\mathbf{n}$  and  $ds$  yield  $dA = -dt d\psi$ , allowing (B 1) to be written as

$$\Delta\psi(\psi, z) = \int_{\psi_m}^{\psi} \int_0^{T(\psi)} \nabla_2 \cdot \mathbf{v} dt d\psi. \tag{B 3}$$

It follows directly from the definitions of  $\Delta\psi$  (B 3) and  $\Delta z$  (4.4) that

$$\frac{\partial \Delta\psi}{\partial \psi} + \frac{\partial \Delta z}{\partial z} = \int_0^{T(\psi)} \left( \nabla_2 \cdot \mathbf{v} + \frac{\partial v_z}{\partial z} \right) dt = \int_0^{T(\psi)} \nabla \cdot \mathbf{v} dt, \quad (\text{B } 4)$$

where  $\nabla$  is the gradient operator in three dimensions. The integrand vanishes identically for incompressible flows  $\mathbf{v}$ , yielding the continuity equation (4.6) in the abstract  $\psi$ - $z$  space, and consequently the Hamiltonian structure of the three-dimensional transport. The derivation for a clockwise vortex follows similarly, bearing in mind that  $\mathbf{n} = -\nabla\psi/|\nabla\psi|$  in this case represents the inward pointing normal. The expression (4.8) for the Hamiltonian  $\mathcal{H}(\psi, z)$  is obtained as  $\mathcal{H} = \int \Delta\psi dz$  using (4.7) and (B 1). It is worth noting that the Hamiltonian formalism developed here formally represents the leading-order modification of two-dimensional trajectories in the limit  $|\mathbf{v}| \ll |\mathbf{u}|$ . The description holds generally for arbitrary time-dependent perturbations  $\mathbf{v}$ , only requiring the condition of incompressibility.

#### REFERENCES

- AHMED, D., MAO, X., SHI, J., JULURI, B. K. & HUANG, T. J. 2009 A millisecond micromixer via single-bubble-based acoustic streaming. *Lab on a Chip* **9** (18), 2738–2741.
- BERTELSEN, A., SVARDAL, A. & TJØTTA, S. 1973 Nonlinear streaming effects associated with oscillating cylinders. *J. Fluid Mech.* **59** (03), 493–511.
- CHONG, K., KELLY, S. D., SMITH, S. & ELDRIDGE, J. D. 2013 Inertial particle trapping in viscous streaming. *Phys. Fluids* **25** (3), 033602.
- CIERPKA, C. & KÄHLER, C. J. 2012 Particle imaging techniques for volumetric three-component (3D3C) velocity measurements in microfluidics. *J. Vis.* **15** (1), 1–31.
- CIERPKA, C., ROSSI, M., SEGURA, R. & KÄHLER, C. J. 2011 On the calibration of astigmatism particle tracking velocimetry for microflows. *Meas. Sci. Technol.* **22** (1), 015401.
- DAVIDSON, B. J. & RILEY, N. 1971 Cavitation microstreaming. *J. Sound Vib.* **15** (2), 217–233.
- DOINIKOV, A. A. 1997 Acoustic radiation force on a spherical particle in a viscous heat-conducting fluid. I. General formula. *J. Acoust. Soc. Am.* **101** (2), 713–721.
- DOINIKOV, A. A. & BOUAKAZ, A. 2010 Acoustic microstreaming around a gas bubble. *J. Acoust. Soc. Am.* **127** (2), 703–709.
- GELDERBLOM, H., ZIJLSTRA, A. G., VAN WIJNGAARDEN, L. & PROSPERETTI, A. 2012 Oscillations of a gas pocket on a liquid-covered solid surface. *Phys. Fluids* **24** (12), 122101.
- HOLTSMARK, J., JOHNSEN, I., SIKKELAND, T. & SKAVLEM, S. 1954 Boundary layer flow near a cylindrical obstacle in an oscillating, incompressible fluid. *J. Acoust. Soc. Am.* **26** (1), 26–39.
- LIGHTHILL, J. 1978 Acoustic streaming. *J. Sound Vib.* **61** (3), 391–418.
- LIU, R. H., YANG, J., PINDER, M. Z., ATHAVALE, M. & GRODZINSKI, P. 2002 Bubble-induced acoustic micromixing. *Lab on a Chip* **2** (3), 151–157.
- LONGUET-HIGGINS, M. S. 1953 Mass transport in water waves. *Phil. Trans. R. Soc. Lond. A* **245** (903), 535–581.
- LONGUET-HIGGINS, M. S. 1970 Viscous streaming from an oscillating spherical bubble. *Proc. R. Soc. Lond. A* **454**, 725–742.
- LUTZ, B. R., CHEN, J. & SCHWARTZ, D. T. 2005 Microscopic steady streaming eddies created around short cylinders in a channel: flow visualization and stokes layer scaling. *Phys. Fluids* **17** (2), 1–7.
- LUTZ, B. R., CHEN, J. & SCHWARTZ, D. T. 2006 Hydrodynamic tweezers: 1. Noncontact trapping of single cells using steady streaming microeddies. *Analyt. Chem.* **78** (15), 5429–5435.
- MARIN, A., ROSSI, M., RALLABANDI, B., WANG, C., HILGENFELDT, S. & KÄHLER, C. J. 2015 Three-dimensional phenomena in microbubble acoustic streaming. *Phys. Rev. Appl.* **3** (4), 041001.

- MARMOTTANT, P. & HILGENFELDT, S. 2003 Controlled vesicle deformation and lysis by single oscillating bubbles. *Nature* **423** (6936), 153–156.
- MARMOTTANT, P. & HILGENFELDT, S. 2004 A bubble-driven microfluidic transport element for bioengineering. *Proc. Natl Acad. Sci. USA* **101** (26), 9523–9527.
- NYBORG, W. L. 1958 Acoustic streaming near a boundary. *J. Acoust. Soc. Am.* **30** (4), 329–339.
- PATEL, M. V., TOVAR, A. R. & LEE, A. P. 2012 Lateral cavity acoustic transducer as an on-chip cell/particle microfluidic switch. *Lab on a Chip* **12** (1), 139–145.
- PHAN, H. V., ŞEŞEN, M., ALAN, T. & NEILD, A. 2014 Single line particle focusing using a vibrating bubble. *Appl. Phys. Lett.* **105** (19), 193507.
- RALLABANDI, B., WANG, C., GUO, L. & HILGENFELDT, S. 2015 Systematic strategies for open flow mixing with microbubble streaming. Preprint.
- RALLABANDI, B., WANG, C. & HILGENFELDT, S. 2014 Two-dimensional streaming flows driven by sessile semicylindrical microbubbles. *J. Fluid Mech.* **739**, 57–71.
- RANEY, W. P., CORELLI, J. C. & WESTERVELT, P. J. 1954 Acoustical streaming in the vicinity of a cylinder. *J. Acoust. Soc. Am.* **26**, 1006–1014.
- RILEY, N. 1965 Oscillating viscous flows. *Mathematika* **12** (02), 161–175.
- RILEY, N. 1966 On a sphere oscillating in a viscous fluid. *Q. J. Mech. Appl. Maths* **19** (4), 461–472.
- RILEY, N. 1967 Oscillatory viscous flows. Review and extension. *IMA J. Appl. Maths* **3** (4), 419–434.
- RILEY, N. 2001 Steady streaming. *Annu. Rev. Fluid Mech.* **33**, 43–65.
- ROGERS, P. & NEILD, A. 2011 Selective particle trapping using an oscillating microbubble. *Lab on a Chip* **11** (21), 3710–3715.
- ROSSI, M. & KÄHLER, C. J. 2014 Optimization of astigmatic particle tracking velocimeters. *Exp. Fluids* **55** (9), 1–13.
- SADHAL, S. S. 2012 Acoustofluidics 16: acoustics streaming near liquid–gas interfaces: drops and bubbles streaming near liquid–gas interfaces: drops and bubbles. *Lab on a Chip* **12** (16), 2771–2781.
- SANZ, A. & DIEZ, J. 1989 Non-axisymmetric oscillations of liquid bridges. *J. Fluid Mech.* **205**, 503–521.
- STUART, J. T. 1966 Double boundary layers in oscillatory viscous flow. *J. Fluid Mech.* **24** (4), 673–687.
- THAMEEM, R., RALLABANDI, B. & HILGENFELDT, S. 2015 Fast sorting of microparticles in bubble streaming flows. Preprint.
- WANG, C. 2013 Microbubble streaming flows for non-invasive particle manipulation and liquid mixing. PhD thesis, University of Illinois at Urbana-Champaign.
- WANG, C., JALIKOP, S. V. & HILGENFELDT, S. 2011 Size-sensitive sorting of microparticles through control of flow geometry. *Appl. Phys. Lett.* **99** (3), 034101.
- WANG, C., JALIKOP, S. V. & HILGENFELDT, S. 2012 Efficient manipulation of microparticles in bubble streaming flows. *Biomicrofluidics* **6** (1), 012801.
- WANG, C., RALLABANDI, B. & HILGENFELDT, S. 2013 Frequency dependence and frequency control of microbubble streaming flows. *Phys. Fluids* **25**, 022002.
- WANG, C.-Y. 1968 On high-frequency oscillatory viscous flows. *J. Fluid Mech.* **32** (01), 55–68.
- WANG, S. S., JIAO, Z. J., HUANG, X. Y., YANG, C. & NGUYEN, N. T. 2009 Acoustically induced bubbles in a microfluidic channel for mixing enhancement. *Microfluid. Nanofluid.* **6** (6), 847–852.
- WIKLUND, M., GREEN, R. & OHLIN, M. 2012 Acoustofluidics 14: applications of acoustic streaming in microfluidic devices. *Lab on a Chip* **12** (14), 2438–2451.
- WU, J. & DU, G. 1997 Streaming generated by a bubble in an ultrasound field. *J. Acoust. Soc. Am.* **101** (4), 1899–1907.
- XIE, Y., AHMED, D., LAPSLEY, M. I., LIN, S.-C. S., NAWAZ, A. A., WANG, L. & HUANG, T. J. 2012 Single-shot characterization of enzymatic reaction constants  $K_m$  and  $k_{cat}$  by an acoustic-driven, bubble-based fast micromixer. *Analyt. Chem.* **84** (17), 7495–7501.